The Astronomical Journal, 160:222 (14pp), 2020 November https://doi.org/10.3847/1538-3881/aba530

HATS-37Ab and HATS-38b: Two Transiting Hot Neptunes in the Desert*

A. Jordán[1,2], G. Á. Bakos[3,4], D. Bayliss[5], J. Bento[6], W. Bhatti[3], R. Brahm[1,2], Z. Csubry[3], N. Espinoza[7], J. D. Hartman[3], Th. Henning[8], L. Mancini[8,9,10], K. Penev[11], M. Rabus[12,13], P. Sarkis[8], V. Suc[1], M. de Val-Borro[14], G. Zhou[15], R. P. Butler[16], J. Teske[17], J. Crane[17], S. Shectman[17], T. G. Tan[18], I. Thompson[17], J. J. Wallace[3], J. Lázár[19], I. Papp[19], and P. Sári[19]

[1] Facultad de Ingeniería y Ciencias, Universidad Adolfo Ibáñez, Av. Diagonal las Torres 2640, Peñalolén, Santiago, Chile; andres.jordan@uai.cl
[2] Millenium Institute of Astrophysics, Santiago, Chile
[3] Department of Astrophysical Sciences, Princeton University, NJ 08544, USA
[4] MTA Distinguished Guest Fellow, Konkoly Observatory, Hungary
[5] Department of Physics, University of Warwick, Coventry CV4 7AL, UK
[6] Research School of Astronomy and Astrophysics, Australian National University, Canberra, ACT 2611, Australia
[7] Space Telescope Science Institute, 3700 San Martin Drive, Baltimore, MD 21218, USA
[8] Max Planck Institute for Astronomy, Königstuhl 17, D-69117—Heidelberg, Germany
[9] Department of Physics, University of Rome Tor Vergata, Via della Ricerca Scientifica 1, I-00133—Roma, Italy
[10] INAF—Astrophysical Observatory of Turin, Via Osservatorio 20, I-10025—Pino Torinese, Italy
[11] Department of Physics, University of Texas at Dallas, Richardson, TX 75080, USA
[12] Las Cumbres Observatory Global Telescope Network, Santa Barbara, CA 93117, USA
[13] Department of Physics, University of California, Santa Barbara, CA 93106-9530, USA
[14] Astrochemistry Laboratory, Goddard Space Flight Center, NASA, 8800 Greenbelt Rd, Greenbelt, MD 20771, USA
[15] Harvard-Smithsonian Center for Astrophysics, 60 Garden St., Cambridge, MA 02138, USA
[16] Earth & Planets Laboratory, Carnegie Institution for Science, Washington DC 20015, USA
[17] The Observatories of the Carnegie Institution for Science, 813 Santa Barbara St, Pasadena, CA 91101, USA
[18] Perth Exoplanet Survey Telescope, Perth, Australia
[19] Hungarian Astronomical Association, 1451 Budapest, Hungary

Received 2020 May 4; revised 2020 July 6; accepted 2020 July 7; published 2020 October 27

Abstract

We report the discovery of two transiting Neptunes by the HATSouth survey. The planet HATS-37Ab has a mass of $0.099 \pm 0.042\,M_{\rm J}$ ($31.5 \pm 13.4\,M_{\oplus}$) and a radius of $0.606 \pm 0.016\,R_{\rm J}$, and is on a $P = 4.3315$ day orbit around a $V = 12.266 \pm 0.030$ mag, $0.843^{+0.017}_{-0.012}\,M_{\odot}$ star with a radius of $0.877^{+0.019}_{-0.012}\,R_{\odot}$. We also present evidence that the star HATS-37A has an unresolved stellar companion HATS-37B, with a photometrically estimated mass of $0.654 \pm 0.033\,M_{\odot}$. The planet HATS-38b has a mass of $0.074 \pm 0.011\,M_{\rm J}$ ($23.5 \pm 3.5\,M_{\oplus}$) and a radius of $0.614 \pm 0.017\,R_{\rm J}$, and is on a $P = 4.3750$ day orbit around a $V = 12.411 \pm 0.030$ mag, $0.890^{+0.016}_{-0.012}\,M_{\odot}$ star with a radius of $1.105 \pm 0.016\,R_{\odot}$. Both systems appear to be old, with isochrone-based ages of $11.46^{+0.79}_{-1.45}$ Gyr, and 11.89 ± 0.60 Gyr, respectively. Both HATS-37Ab and HATS-38b lie in the Neptune desert and are thus examples of a population with a low occurrence rate. They are also among the lowest-mass planets found from ground-based wide-field surveys to date.

Unified Astronomy Thesaurus concepts: Exoplanets (498); Hot Neptunes (754)

Supporting material: machine-readable tables

1. Introduction

Over the past two decades the population of known transiting exoplanets has grown at an accelerating pace, with the Kepler satellite (Borucki et al. 2010) dominating the overall number of discoveries. The distribution of the discoveries is far from homogeneous in terms of the planetary parameters, both due to observational biases and variations in the intrinsic occurrence of planets as a function of their physical parameters and those of their host stars. An example of an observational bias is the paucity of known transiting exoplanets with periods $P \gtrsim 10$ days, a region of parameter space that the ground-based survey HATSouth (Bakos et al. 2013) was designed to target, and that is currently being explored efficiently by the Transiting Exoplanet Survey Satellite mission (TESS, Ricker et al. 2015). An example of intrinsically low occurrence rates is the so-called *Neptune desert*, a term coined by Mazeh et al. (2016) to describe a wedge in the period-mass or period–radius diagram where close-in ($P \lesssim 5$ days) planets with radii similar to Neptune are very rare, and essentially nonexistent for $P \lesssim 3$ days (see also Szabó & Kiss 2011; Beaugé & Nesvorný 2013).

In order to uncover more planetary systems in sparsely populated regions such as the Neptune desert it pays to survey to fainter magnitudes than what TESS is optimized for. Ground-based wide-field surveys that are currently in operation, such as HATSouth or NGTS (Wheatley et al. 2018), can complement TESS by uncovering an additional

* The HATSouth network is operated by a collaboration consisting of Princeton University (PU), the Max Planck Institute für Astronomie (MPIA), the Australian National University (ANU), and Universidad Adolfo Ibáñez (UAI). The station at Las Campanas Observatory of the Carnegie Institution for Science is operated by PU in conjunction with UAI, the station at the High Energy Spectroscopic Survey site is operated in conjunction with MPIA, and the station at Siding Spring Observatory (SSO) is operated jointly with ANU. This work is based in part on observations made with the MPG 2.2 m Telescope at the ESO Observatory in La Silla and based on observations collected at the European Southern Observatory under ESO programmes 094.C-0428(A), 095.C-0367(A), 097.C-0571(A), 098.C-0292(A), 099.C-0374(A), 0100.C-0406(A), 0100.C-0406(B). This paper includes data gathered with the 6.5 m Magellan Telescopes at Las Campanas Observatory, Chile, and is based in part on observations made with the Anglo-Australian Telescope operated by the Australian Astronomical Observatory.

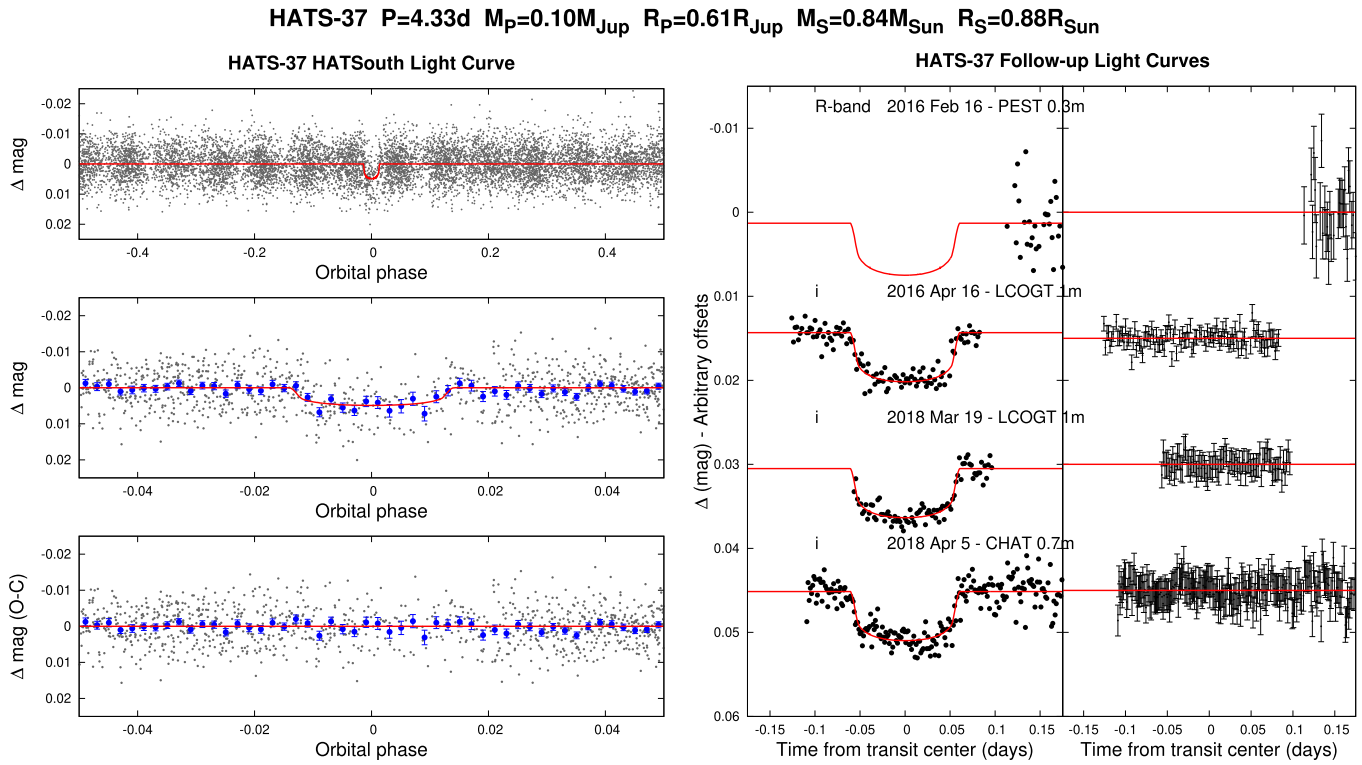

Figure 1. Observations used to confirm the transiting planet system HATS-37. Top left: phase-folded unbinned HATSouth light curve. The top panel shows the full light curve, the middle panel shows the light curve zoomed in on the transit, and the bottom panel shows the residuals from the best-fit model zoomed in on the transit. The solid lines show the model fits to the light curves. The dark filled circles show the light curves binned in phase with a bin size of 0.002. Top right: unbinned follow-up transit light curves corrected for instrumental trends fitted simultaneously with the transit model, which is overplotted. The dates, filters, and instruments used are indicated. The residuals are shown on the right side in the same order as the original light curves. The error bars represent the photon and background shot noise, plus the readout noise. Note that these uncertainties are scaled up in the fitting procedure to achieve a reduced χ^2 of unity, but the uncertainties shown in the plot have not been scaled. Bottom left: high-precision RVs phased with respect to the midtransit time. The instruments used are labeled in the plot. The top panel shows the phased measurements together with the best-fit model. The center-of-mass velocity has been subtracted. Both the observations and the model have also had a linear trend in time subtracted (Figure 5). In this case the model has not been corrected for dilution from the unresolved stellar component HATS-37B. We find that the dilution corrected orbit has a semiamplitude that is ∼20% larger than what is shown here. The second panel shows the velocity $O - C$ residuals. The error bars include the estimated jitter. The third panel shows the bisector spans. Bottom right: color–magnitude diagram (CMD) and spectral energy distribution (SED). The top panel shows the absolute G magnitude vs. the dereddened $BP - RP$ color compared to theoretical isochrones (black lines) and stellar evolution tracks (green lines) from the PARSEC models interpolated at the best-estimate value for the metallicity of the host. The age of each isochrone is listed in black in gigayears, while the mass of each evolution track is listed in green in solar mass units. The filled blue circles show the measured reddening- and distance-corrected values from Gaia DR2, while the blue lines indicate the 1σ and 2σ confidence regions, including the estimated systematic errors in the photometry. Here we model the system as a binary star with a planet transiting one component. The 1σ posterior distributions for the primary star HATS-37A and secondary star HATS-37B are shown as red ellipses. The gray ellipse shows the 1σ posterior distribution for the combined photometry of the system. The inset shows a zoomed-in view around the primary star and the combined photometry. The middle panel shows the SED as measured via broadband photometry through the listed filters. Here we plot the observed magnitudes with mass 0.84 $M_\odot$, and a secondary star with mass 0.65 $M_\odot$. The second mode consists of a primary star with mass 0.88 $M_\odot$, and a fainter secondary star with mass 0.48 $M_\odot$. The first mode is ∼35 times more likely based on its representation in the posterior distribution. The model makes use of the predicted absolute magnitudes in each bandpass from the PARSEC isochrones, the distance to the system (constrained largely via Gaia DR2) and extinction (constrained from the SED with a prior coming from the MWDUST 3D Galactic extinction model). The bottom panel shows the $O - C$ residuals from the best-fit model SED.

number of intrinsically rare systems. Indeed, one of the most extreme systems in the Neptune desert was recently uncovered by the NGTS (NGTS4-b, West et al. 2019). The reason for the existence of the desert is under investigation. The physical processes thought to be relevant are photo-evaporation and the tidal disruption barrier for gas giants after high-eccentricity migration (see Owen & Lai 2018, and references therein).

In this paper we report the discovery by the HATSouth survey of two transiting Neptunes in the desert. They both have similar radii and period values, and fairly similar masses. We thus contribute two more systems to the sparsely populated Neptune desert. The paper is structured as follows. In Section 2 we describe the observational data that were used to perform the modeling of the system as described in Section 3. The results are discussed in Section 4.

2. Observations

Figures 1 and 2 show the observations collected for HATS-37 and HATS-38, respectively. Each figure shows the HATSouth light curve used to detect the transits, the ground-based follow-up transit light curves, the high-precision radial velocities (RVs) and spectral line bisector spans (BSs), and the catalog broadband photometry, including parallax corrections from Gaia DR2, used for characterizing the host stars. Below we describe the observations of these objects that were collected by our team.

2.1. Photometric Detection

Both of the systems presented here were initially detected as transiting planet candidates based on observations by the HATSouth network. The operations of the network are

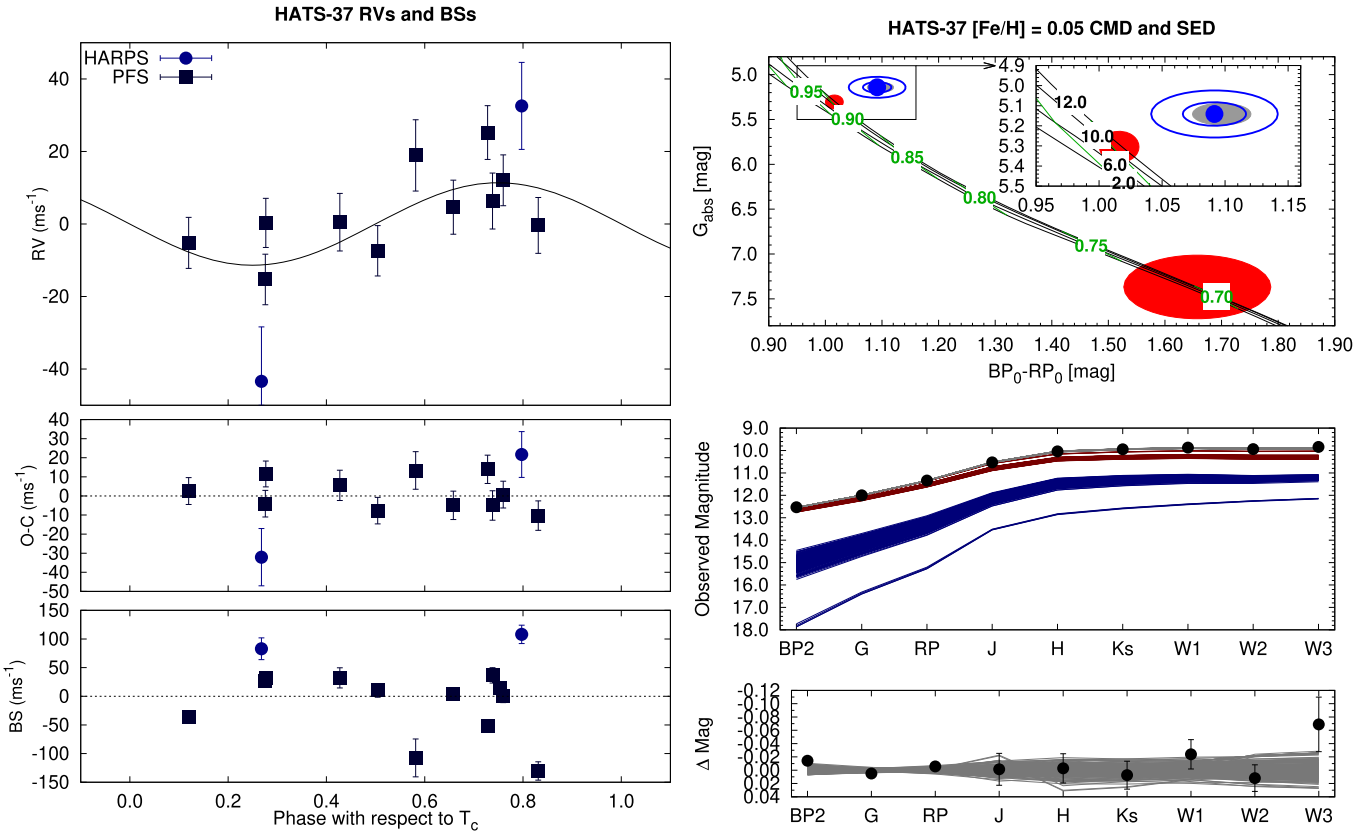

Figure 1. (Continued.)

described in Bakos et al. (2013), while our methods for reducing the data to trend-filtered light curves (filtered using the method of Kovács et al. 2005) and identifying transiting planet signals (using the Box-fitting Least Squares or BLS method; Kovács et al. 2002) are described in Penev et al. (2013). The HATSouth observations of each system are summarized in Table 1, while the light curve data are made available in Table 3.

We also searched the light curves for other periodic signals using the generalized Lomb–Scargle method (Zechmeister & Kürster 2009), and for additional transit signals by applying a second iteration of BLS. Both of these searches were performed on the residual light curves after subtracting the best-fit primary transit models. No additional periodic signals are detected for HATS-37. For HATS-38 we detect a periodic signal at a period of $P = 21.52$ days, semiamplitude of 0.43 mmag, and a false alarm probability, determined via bootstrap simulations, of $10^{-6.3}$. We do not detect any additional transit signals in its light curve. The periodic signal detected for HATS-38 may correspond to the photometric rotation period of this $T_{\rm eff} = 5740 \pm 50$ K star. The star has $v \sin i = 3.10 \pm 0.27$ km s^{-1}, which gives an upper limit of 18.7 ± 1.7 days on the equatorial rotation period. The photometric period of 21.52 days is 1.7σ larger than this upper limit, but a larger value is possible if the rotation axis has $\sin i \approx 1$ and the spots are at a latitude that is rotating more slowly than the equator.

2.2. Spectroscopic Observations

The spectroscopic observations carried out to confirm and characterize both of the transiting planet systems are summarized in Table 2. The facilities used include FEROS on the MPG 2.2 m (Kaufer & Pasquini 1998), Coralie on the Euler 1.2 m (Queloz et al. 2001), HARPS on the ESO 3.6 m (Mayor et al. 2003), WiFeS on the ANU 2.3 m (Dopita et al. 2007), and PFS on the Magellan 6.5 m (Crane et al. 2006, 2008, 2010).

The FEROS, Coralie, and HARPS observations were reduced to wavelength-calibrated spectra and high-precision RV and bisector span (BS) measurements using the CERES pipeline (Brahm et al. 2017a).

The WiFeS observations of HATS-37, which were used for reconnaissance, were reduced following Bayliss et al. (2013). We obtained a single spectrum at resolution $R \equiv \Delta\lambda/\lambda \approx 3000$ from which we estimated the effective temperature, $\log g$ and [Fe/H] of the star. Three observations at $R \approx 7000$ were also obtained to search for any large amplitude RV variations at the $\sim$4 km s^{-1} level, which would indicate a stellar mass companion.

The PFS observations of both HATS-37 and HATS-38 include observations through an I_2 cell, and observations without the cell used to construct a spectral template. The observations were reduced to spectra and used to determine high-precision relative RV measurements following Butler et al. (1996). Spectral line bisector spans and their uncertainties were measured as described by Jordán et al. (2014) and Brahm et al. (2017a).

We also used the HARPS and I_2-free PFS observations to determine high-precision stellar atmospheric parameters, including the effective temperature $T_{\rm eff\star}$, surface gravity $\log g$, metallicity [Fe/H], and $v \sin i$ via the ZASPE package (Brahm et al. 2017b). For HATS-37 we used the PFS observations to

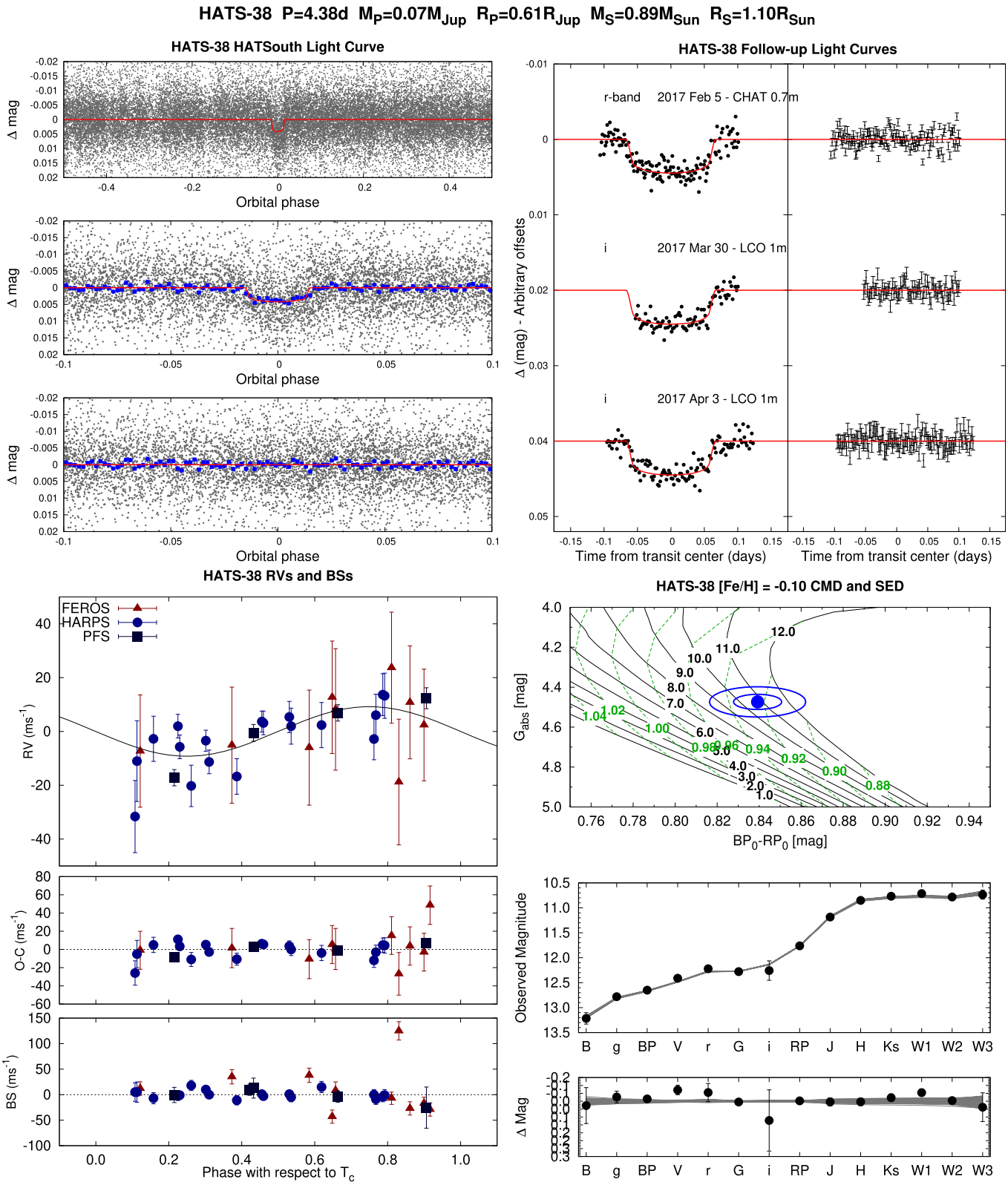

Figure 2. Same as Figure 1. Here we show the observations of HATS-38 when it is modeled as a single star with a transiting planet.

perform this analysis, while for HATS-38 this analysis was performed on the HARPS observations.

The high-precision RV and BS measurements are given in Table 4 for both systems.

2.3. Photometric Follow-up Observations

Follow-up higher-precision ground-based photometric transit observations were obtained for both systems, as summarized in Table 1. The facilities used for this purpose include: the

Table 1
Summary of Photometric Observations

Instrument/Field[a]	Date(s)	# Images	Cadence[b] (s)	Filter	Precision[c] (mmag)
HATS-37					
HS-1/G567.1	2011 Mar–2011 Aug	4975	294	r	5.2
HS-3/G567.1	2011 Jul–2011 Aug	735	297	r	5.7
HS-5/G567.1	2011 Mar–2011 Aug	3217	291	r	5.0
PEST 0.3 m	2016 Feb 16	113	132	R_C	2.8
Swope 1 m/e2v	2017 Apr 4	161	104	i	1.6
LCO 1 m/sinistro	2016 Apr 16	108	159	i'	1.0
LCO 1 m/sinistro	2018 Mar 19	82	163	i'	0.8
CHAT 0.7 m	2018 Apr 5	217	113	i	1.4
HATS-38					
HS-1/G561.1	2014 Dec–2015 Jul	4892	319	r	6.7
HS-2/G561.1	2014 Dec–2015 Jul	5718	349	r	4.7
HS-3/G561.1	2014 Dec–2015 Jul	3691	353	r	5.1
HS-4/G561.1	2014 Dec–2015 Jul	2862	352	r	6.9
HS-5/G561.1	2014 Dec–2015 Jul	2959	356	r	5.7
HS-6/G561.1	2014 Dec–2015 Jul	3058	342	r	6.9
HS-1/G561.1.focus	2014 Dec–2015 Jul	2026	1122	r	14.5
HS-2/G561.1.focus	2014 Dec–2015 Jul	2134	1204	r	13.4
HS-3/G561.1.focus	2014 Dec–2015 Jul	1217	1227	r	14.1
HS-4/G561.1.focus	2014 Dec–2015 Jul	977	1221	r	15.5
HS-5/G561.1.focus	2014 Dec–2015 Jul	1190	1232	r	15.0
HS-6/G561.1.focus	2014 Dec–2015 Jul	1174	1206	r	15.7
CHAT 0.7 m	2017 Feb 5	146	112	r	1.1
LCO 1 m/sinistro	2017 Mar 30	83	161	i'	0.9
LCO 1 m/sinistro	2017 Apr 3	118	160	i'	1.0

Notes.
[a] For HATSouth data we list the HATSouth unit, CCD, and field name from which the observations are taken. HS-1 and -2 are located at Las Campanas Observatory in Chile, HS-3 and -4 are located at the High Energy Spectroscopic Survey site in Namibia, and HS-5 and -6 are located at Siding Spring Observatory in Australia. Each unit has four CCDs. Each field corresponds to 1 of 838 fixed pointings used to cover the full 4π celestial sphere. All data from a given HATSouth field and CCD number are reduced together, while detrending through external parameter decorrelation (EPD) is done independently for each unique unit+CCD+field combination. For HATS-38 we also derived light curves from short (30 s) focus frames that were taken by the HATSouth instruments every ~20 minutes. The Swope 1 m light curve for HATS-37 covered a predicted secondary eclipse event.
[b] The median time between consecutive images rounded to the nearest second. Due to factors such as weather, the day–night cycle, and guiding and focus corrections the cadence is only approximately uniform over short timescales.
[c] The rms of the residuals from the best-fit model.

Chilean-Hungarian Automated Telescope (CHAT) 0.7 m telescope at Las Campanas Observatory, Chile (A. Jordán et al. 2018, in preparation); 1 m telescopes from the Las Cumbres Observatory (LCO) network, (Brown et al. 2013); the 0.3 m Perth Exoplanet Survey Telescope in Australia (PEST);[20] and the Swope 1 m telescope at Las Campanas Observatory in Chile.

Our methods for carrying out the observations with these facilities and reducing the data to light curves are described in our previous papers (Bayliss et al. 2013; Mohler-Fischer et al. 2013; Penev et al. 2013; Jordán et al. 2014; Hartman et al. 2015, 2019; Rabus et al. 2016).

The time-series photometry data are available in Table 3, and are plotted for each object in Figures 1 and 2.

2.4. TESS Light Curves

During its primary mission, TESS observed both of our targets. HATS-37 (TIC6036597) was observed on Sector 10, CCD 3 of camera 1, but the source lies within the bleed of a nearby bright star, making the photometry unusable. HATS-38 (TIC168281028) was observed by the TESS primary mission during its first year of operations. The target star fell on Camera 2, CCD 4 of the Sector 9 observations. Photometry was extracted from the Science Processing Operations Center (SPOC Jenkins et al. 2016) calibrated Full Frame Images (FFIs), retrieved via the MAST *tesscut* tool. Aperture photometry was performed using selected pixels of a 7 × 7 pixel cutout of the FFIs with the *lightkurve* package (Barentsen et al. 2019). The background flux was estimated from the remainder pixels that excluded nearby stars. We corrected for the flux contribution from nearby stars within our photometric aperture. A list of nearby stars was queried from the TICv8 catalog (Stassun et al. 2019), and their flux contributions to the photometric aperture were computed assuming each star has a Gaussian profile with FWHM of 1.63 pixels, as measured from the TESS pixel response function at the location of the target star. The TESS light curve for HATS-38 is shown in Figure 3.

2.5. Search for Resolved Stellar Companions

The Gaia DR2 catalog provides the highest spatial resolution optical imaging for both of these targets. Gaia DR2 is sensitive

[20] http://pestobservatory.com/

Table 2
Summary of Spectroscopy Observations

Instrument	UT Date(s)	# Spec.	Res. $\Delta\lambda/\lambda/1000$	S/N Range[a]	γ_{RV}[b] (km s^{-1})	RV Precision[c] (m s^{-1})
HATS-37						
ANU 2.3 m/WiFeS	2014 Feb 20	1	3	35	…	…
ANU 2.3 m/WiFeS	2014 Feb 20–23	3	7	38–72	8.2	4000
Euler 1.2 m/Coralie	2014 Mar–2016 Jun	6	60	20–29	7.05	149
ESO 3.6 m/HARPS	2016 Feb 27–29	2	115	19–22	6.417	38
Magellan 6.5 m/PFS+I_2	2016 Jun–2017 Apr	11	76	…	…	8.7
Magellan 6.5 m/PFS	2016 Jun 20	1	76	…	…	…
HATS-38						
Euler 1.2 m/Coralie	2016 Nov 16–18	3	60	17–20	4.143	54
ESO 3.6 m/HARPS	2016 Nov–2017 May	18	115	17–47	4.144	9.2
MPG 2.2 m/FEROS	2016 Dec–2017 Mar	10	48	36–67	4.130	19
Magellan 6.5 m/PFS+I_2	2017 Apr 5–8	4	76	…	…	5.7
Magellan 6.5 m/PFS	2017 Apr 19	1	76	…	…	…

Notes.
[a] Signal-to-noise ratio (S/N) per resolution element near 5180 Å. This was not measured for all of the instruments.
[b] For high-precision RV observations included in the orbit determination this is the zeropoint RV from the best-fit orbit. For other instruments it is the mean value. We only provide this quantity when applicable.
[c] For high-precision RV observations included in the orbit determination this is the scatter in the RV residuals from the best-fit orbit (which may include astrophysical jitter), for other instruments this is either an estimate of the precision (not including jitter), or the measured standard deviation. We only provide this quantity when applicable.

Table 3
Light Curve Data for HATS-37 and HATS-38

Object[a]	BJD[b]	Mag[c]	σ_{Mag}	Mag(orig)[d]	Filter	Instrument
HATS-37	2455765.23265	0.00383	0.00267	…	*r*	HS
HATS-37	2455691.59689	−0.00538	0.00294	…	*r*	HS
HATS-37	2455678.60275	0.00353	0.00337	…	*r*	HS
HATS-37	2455747.90786	0.00160	0.00295	…	*r*	HS
HATS-37	2455682.93494	−0.00208	0.00250	…	*r*	HS
HATS-37	2455665.61003	−0.00583	0.00305	…	*r*	HS
HATS-37	2455708.92562	0.00583	0.00249	…	*r*	HS
HATS-37	2455691.60029	0.00317	0.00300	…	*r*	HS
HATS-37	2455652.61745	−0.00718	0.00291	…	*r*	HS
HATS-37	2455747.91127	0.00013	0.00262	…	*r*	HS

Notes.
[a] Either HATS-37 or HATS-38.
[b] Barycentric Julian date is computed directly from the UTC time without correction for leap seconds.
[c] The out-of-transit level has been subtracted. For observations made with the HATSouth instruments (identified by "HS" in the "Instrument" column) these magnitudes have been corrected for trends using the EPD and TFA procedures applied *prior* to fitting the transit model. This procedure may lead to an artificial dilution in the transit depths. The blend factors for the HATSouth light curves are listed in Table 7. For observations made with follow-up instruments (anything other than "HS" in the "Instrument" column), the magnitudes have been corrected for a quadratic trend in time, and for variations correlated with up to three PSF shape parameters, fit simultaneously with the transit.
[d] Raw magnitude values without correction for the quadratic trend in time, or for trends correlated with the seeing. These are only reported for the follow-up observations.

(This table is available in its entirety in machine-readable form.)

to neighbors with $G \lesssim 20$ mag down to a limiting resolution of $\sim 1''$ (e.g., Ziegler et al. 2018). We find that neither object has a resolved neighbor in the Gaia DR2 catalog within $10''$.

For HATS-38 we also obtained J and K_S-band images using the WIYN High-Resolution Infrared Camera (WHIRC) on the WIYN 3.5 m telescope at Kitt Peak National Observatory (KPNO) in Arizona. The observations were carried out on the night of 2018 March 18, and have an effective FWHM of $0.''43$ in J and $0.''35$ in K_S. The images were collected at four different node positions in each filter. These were calibrated, background-subtracted, registered, and median-combined using the FITSH software package (Pál 2012).

We find a faint source separated from HATS-38 by $6''$. The source is detected at about $\sim 3\sigma$ confidence in both bands, and has a magnitude contrast of $\Delta J = 8.05 \pm 0.09$ mag and $\Delta K_s = 7.18 \pm 0.08$ mag compared to HATS-38. The object is too faint, and too distant from HATS-38 to be responsible for the transit signal. The J and K_s magnitudes are consistent with

Table 4
Relative Radial Velocities and Bisector Spans for HATS-37 and HATS-38

System	BJD (2,450,000+)	RV[a] (m s^{-1})	σ_{RV}[b] (m s^{-1})	BS (m s^{-1})	σ_{BS} (m s^{-1})	Phase	Instrument
HATS-37							
HATS-37	7505.50363	−43.39	15.00	83.0	19.0	0.268	HARPS
HATS-37	7507.79700	32.57	12.00	108.0	16.0	0.797	HARPS
HATS-37	7557.51991	0.29	2.71	31.5	10.7	0.277	PFS
HATS-37	7559.58237	...	...	15.2	8.4	0.753	PFS
HATS-37	7559.61286	12.06	3.25	0.0	11.2	0.760	PFS
HATS-37	7614.48266	0.50	4.95	32.2	17.6	0.427	PFS
HATS-37	7615.48351	4.63	4.11	3.8	10.5	0.658	PFS
HATS-37	7617.48123	−5.21	3.30	−36.9	10.0	0.120	PFS
HATS-37	7619.48263	18.92	7.62	−107.5	33.0	0.582	PFS
HATS-37	7622.48860	−15.30	3.16	27.1	11.4	0.276	PFS
HATS-37	7623.47962	−7.39	3.12	10.3	11.8	0.504	PFS
HATS-37	7624.49150	6.33	4.59	36.5	13.4	0.738	PFS
HATS-37	7849.68766	25.22	4.06	−52.0	10.3	0.728	PFS
HATS-37	7858.79784	−0.39	4.54	−130.3	16.1	0.831	PFS
HATS-38							
HATS-38	7708.80458	−23.72	7.70	18.0	10.0	0.262	HARPS
HATS-38	7736.74573	9.76	8.60	−43.0	13.0	0.648	FEROS
HATS-38	7737.84703	−0.54	8.20	−17.0	12.0	0.900	FEROS
HATS-38	7740.84458	−8.94	9.70	38.0	14.0	0.585	FEROS
HATS-38	7741.83263	20.76	7.90	−7.0	12.0	0.811	FEROS
HATS-38	7759.79504	50.26	9.00	−29.0	13.0	0.917	FEROS
HATS-38	7804.60303	−6.22	8.40	−7.0	11.0	0.158	HARPS
HATS-38	7805.54338	−8.04	10.10	35.0	14.0	0.373	FEROS
HATS-38	7805.60189	−20.22	6.60	−11.0	9.0	0.387	HARPS
HATS-38	7806.61869	−1.12	8.40	15.0	11.0	0.619	HARPS
HATS-38	7806.78686	5.26	12.10	8.0	17.0	0.658	FEROS
HATS-38	7807.54628	−21.74	13.50	125.0	18.0	0.831	FEROS
HATS-38	7829.55448	7.86	8.80	−27.0	13.0	0.862	FEROS
HATS-38	7830.69385	−10.24	8.50	12.0	13.0	0.122	FEROS
HATS-38	7848.60266	−18.23	3.02	−0.5	14.9	0.215	PFS
HATS-38	7849.55287	−1.57	3.11	12.9	19.6	0.433	PFS
HATS-38	7850.56508	5.85	3.02	−3.7	11.4	0.664	PFS
HATS-38	7851.62685	11.30	3.89	−25.4	40.4	0.907	PFS
HATS-38	7862.63029	...	...	9.0	10.3	0.422	PFS
HATS-38	7866.48140	−6.92	3.90	10.0	5.0	0.302	HARPS
HATS-38	7866.52106	−14.82	4.40	0.0	6.0	0.311	HARPS
HATS-38	7867.48250	1.88	5.80	1.0	7.0	0.531	HARPS
HATS-38	7867.50397	−1.52	6.70	−5.0	9.0	0.536	HARPS
HATS-38	7868.49777	−6.32	7.70	0.0	10.0	0.763	HARPS
HATS-38	7868.52092	2.58	7.80	−9.0	10.0	0.768	HARPS
HATS-38	7870.52143	−1.52	4.40	−3.0	6.0	0.225	HARPS
HATS-38	7870.54312	−9.22	4.40	−1.0	6.0	0.230	HARPS
HATS-38	7871.52764	0.18	3.90	1.0	5.0	0.455	HARPS
HATS-38	7871.54726	−0.32	4.40	−3.0	6.0	0.460	HARPS
HATS-38	7887.50781	−35.12	13.40	5.0	18.0	0.108	HARPS
HATS-38	7887.53008	−14.52	15.00	5.0	20.0	0.113	HARPS
HATS-38	7890.47840	10.18	7.80	−4.0	10.0	0.787	HARPS
HATS-38	7890.50175	9.78	8.40	−1.0	11.0	0.792	HARPS

Notes.
[a] The zeropoint of these velocities is arbitrary. An overall offset γ_{rel} fitted independently to the velocities from each instrument has been subtracted.
[b] Internal errors excluding the component of astrophysical jitter are listed in Table 7.

(This table is available in its entirety in machine-readable form.)

it being a 0.09 $M_{\odot}$ star that is physically bound to HATS-38, at a current projected separation of ∼2100 au. In that case the source would have $G \sim 23$ mag, consistent with the object not being included in Gaia DR2. It could also be an extragalactic source, an earlier M dwarf star that is in the background of HATS-38, or a foreground brown dwarf.

No other sources are detected closer to HATS-38 in the WIYN/WHIRC images. Figure 4 shows the resulting 5σ contrast curves for HATS-38. These curves were generated using the tools described by Espinoza et al. (2016). We can rule out neighbors with $\Delta J < 3$ mag and $\Delta K_s < 3$ mag at a separation of 0.″5, and $\Delta J < 7$ mag and $\Delta K_s < 6$ mag at a separation of 1.″5.

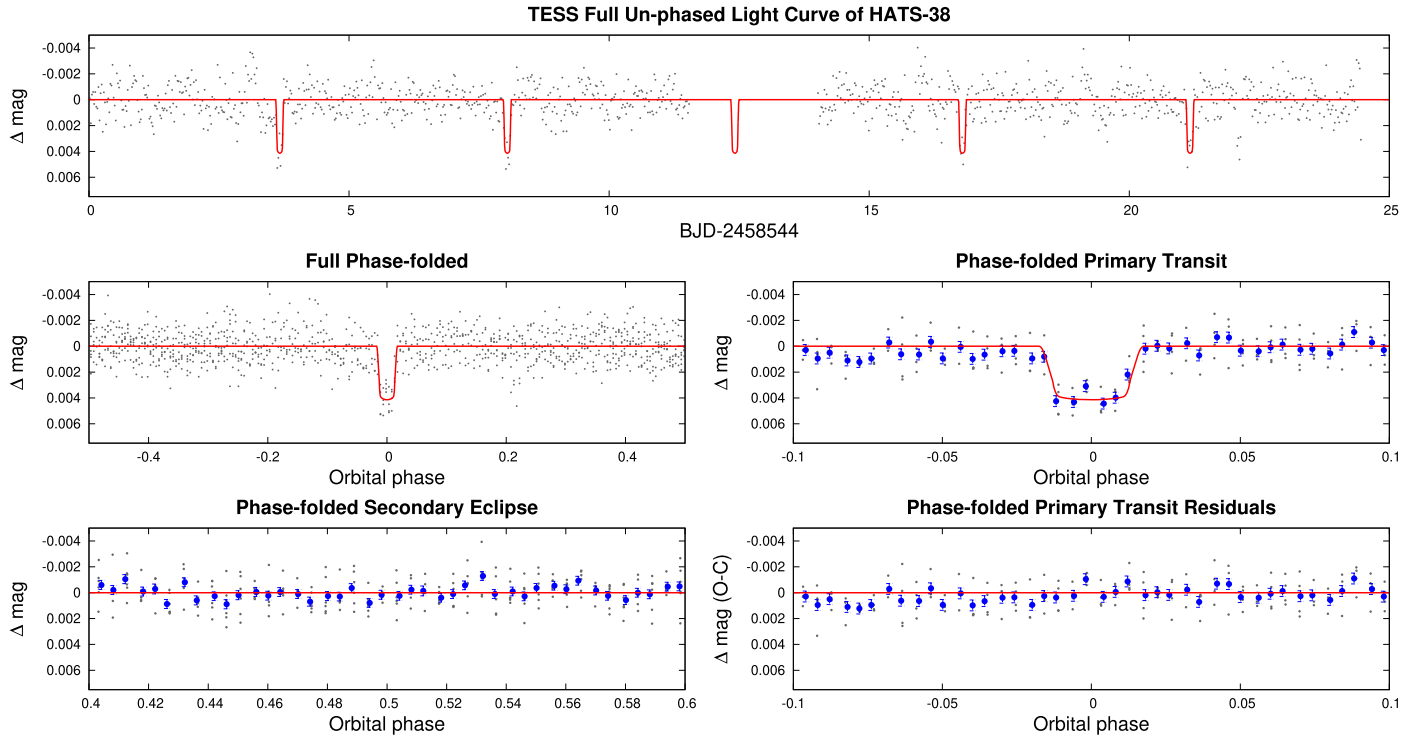

Figure 3. Top: unbinned TESS observations of HATS-38 plotted against time simultaneously with the transit model, which is overplotted. Middle: phase-folded unbinned TESS light curve. The left panel shows the full light curve, and the right panel shows the light curve zoomed in on the transit. The solid lines show the model fits to the light curves. The blue filled circles in the middle right panel show the light curve binned in phase with a bin size of 0.002. Bottom: phase-folded TESS light curve around the predicted time of secondary eclipse (left panel) and residuals with respect to the transit model shown in the middle right panel. The black dots show the unbinned data, while the blue filled circle show values binned in phase with a bin size of 0.002.

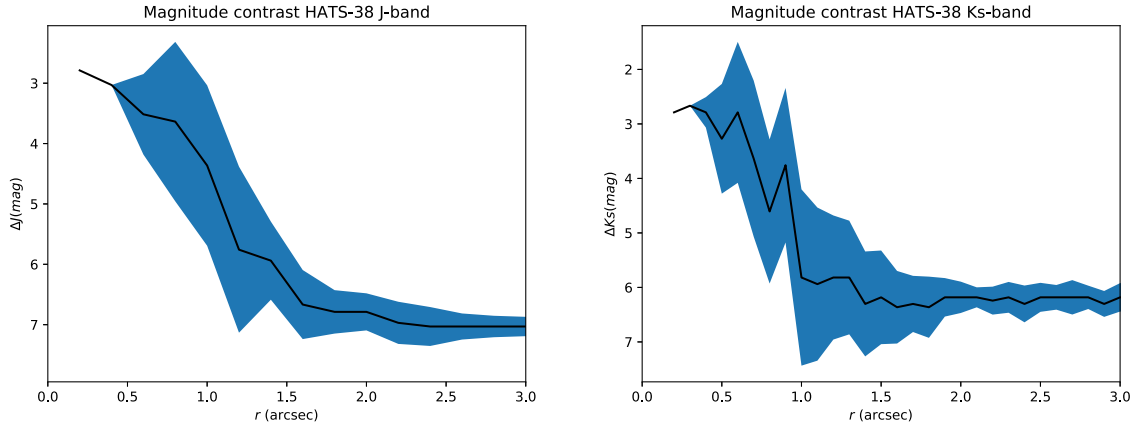

Figure 4. 5σ contrast curve for HATS-38 based on our WIYN/WHIRC J-band (left) and K_S-band (right) observations. In each case the blue band shows the variation in the limit in azimuth at a given radius.

3. Analysis

We analyzed the photometric and spectroscopic observations of each system to determine the stellar and planetary parameters following the methods described in Hartman et al. (2019), with modifications as summarized most recently in Bakos et al. (2020). Briefly, the modeling involves performing a global fit of all the light curves and RV curves described in Section 2, spectroscopically measured stellar atmospheric parameters, catalog broadband photometry, and stellar parallax using a differential evolution Markov Chain Monte Carlo (DEMCMC) method. We fit the observations in two modes: (1) using an empirical method to determine the stellar mass given the direct observational constraint on the stellar radius and bulk density; and (2) constraining the stellar physical parameters using the PARSEC stellar evolution models (Marigo et al. 2017). We use the MWDUST Galactic extinction model (Bovy et al. 2016) to place a prior constraint on the line-of-sight extinction, but we allow the value to vary in the fit.

We also performed a blend model of each system following Hartman et al. (2019), where we attempt to fit all of the observations, except the RV data, using various combinations of stars, with parameters constrained by the PARSEC models. This is done both to rule out blended stellar eclipsing binary scenarios, and to identify systems that may have an unresolved

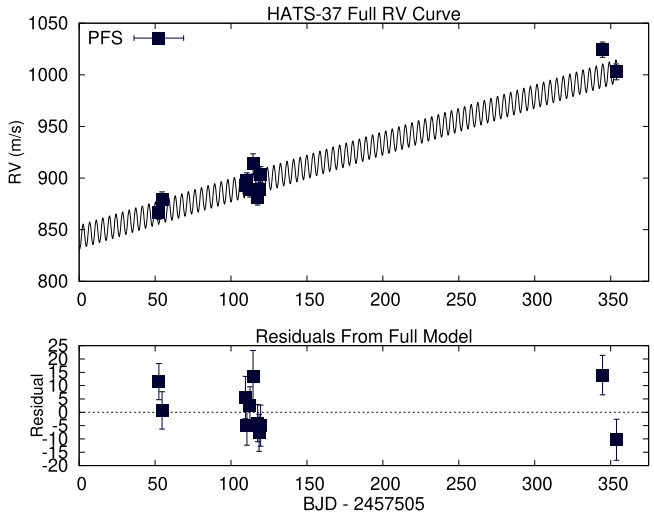

Figure 5. Top: RV observations of HATS-37 plotted against time. The solid line shows the best-fit model including a linear trend and the Keplerian orbital variation of the host star due to the planet HATS-37Ab. As in Figure 1, the RV model plotted here is not corrected for dilution from the unresolved stellar component HATS-37B. The corrected semiamplitude of the orbit is ∼20% larger than what is shown. Bottom: RV residuals from the best-fit model plotted against time.

Table 5
Astrometric, Spectroscopic, and Photometric Parameters for HATS-37 and HATS-38

Parameter	HATS-37 Value	HATS-38 Value	Source
Astrometric properties and cross-identifications			
2MASS-ID	13191246–2259127	10170509–2516345	
GAIA DR2-ID	6194574671813047424	5472386851683941376	
TIC-ID	6036597	168281028	
R.A. (J2000)	$13^{h}19^{m}12\overset{s}{.}4637$	$10^{h}17^{m}05\overset{s}{.}0796$	GAIA DR2
Decl. (J2000)	$-22°59'12\overset{''}{.}7306$	$-25°16'34\overset{''}{.}5568$	GAIA DR2
$\mu_{\rm R.A.}$ (mas yr^{-1})	-21.78 ± 0.11	-21.752 ± 0.066	GAIA DR2
$\mu_{\rm decl.}$ (mas yr^{-1})	6.15 ± 0.11	-7.540 ± 0.070	GAIA DR2
parallax (mas)	4.692 ± 0.061	2.883 ± 0.043	GAIA DR2
Spectroscopic properties			
$T_{\rm eff\star}$ (K)	5247 ± 50	5740 ± 50	ZASPE[a]
[Fe/H]	0.040 ± 0.030	0.060 ± 0.026	ZASPE
$v \sin i$ (km s^{-1})	3.98 ± 0.30	3.10 ± 0.27	ZASPE
$v_{\rm mac}$ (km s^{-1})	3.175 ± 0.076	3.934 ± 0.076	Assumed
$v_{\rm mic}$ (km s^{-1})	0.818 ± 0.023	1.059 ± 0.028	Assumed
$\gamma_{\rm RV}$ (m s^{-1})	6417 ± 0	4144.0 ± 1.5	HARPS[b]
Photometric properties			
G (mag)[c]	11.99780 ± 0.00020	12.27810 ± 0.00020	GAIA DR2
BP (mag)[c]	12.5309 ± 0.0023	12.6494 ± 0.0012	GAIA DR2
RP (mag)[c]	11.3387 ± 0.0017	11.76070 ± 0.00060	GAIA DR2
B (mag)	13.222 ± 0.060	13.22 ± 0.11	APASS[d]
V (mag)	12.266 ± 0.030	12.411 ± 0.030	APASS[d]
g (mag)	12.733 ± 0.060	12.780 ± 0.037	APASS[d]
r (mag)	11.906 ± 0.030	12.220 ± 0.057	APASS[d]
i (mag)	11.616 ± 0.030	12.26 ± 0.19	APASS[d]
J (mag)	10.528 ± 0.024	11.184 ± 0.026	2MASS
H (mag)	10.038 ± 0.022	10.850 ± 0.024	2MASS
K_s (mag)	9.947 ± 0.021	10.768 ± 0.024	2MASS
$W1$ (mag)	9.866 ± 0.022	10.714 ± 0.023	*WISE*
$W2$ (mag)	9.942 ± 0.021	10.783 ± 0.022	*WISE*
$W3$ (mag)	9.896 ± 0.047	10.736 ± 0.091	*WISE*

Notes.
[a] ZASPE = zonal atmospherical stellar parameter estimator routine for the analysis of high-resolution spectra (Brahm et al. 2017b), applied to the FEROS spectra of each system. These parameters rely primarily on ZASPE, but have a small dependence also on the iterative analysis incorporating the isochrone search and global modeling of the data.
[b] The error on $\gamma_{\rm RV}$ is determined from the orbital fit to the RV measurements, and does not include the systematic uncertainty in transforming the velocities to the IAU standard system. The velocities have not been corrected for gravitational redshifts.
[c] The listed uncertainties for the Gaia DR2 photometry are taken from the catalog. For the analysis we assume additional systematic uncertainties of 0.002 mag, 0.005 mag and 0.003 mag for the G, BP, and RP bands, respectively.
[d] From APASS DR6, as listed in the UCAC 4 catalog (Zacharias et al. 2013).

Table 6
Adopted Derived Stellar Parameters for HATS-37 and HATS-38

Parameter	HATS-37 Value	HATS-38 Value
Planet Hosting Star HATS-37A and HATS-38		
$M_\star$ ($M_\odot$)	$0.843^{+0.017}_{-0.012}$	$0.890^{+0.016}_{-0.012}$
$R_\star$ ($R_\odot$)	$0.877^{+0.019}_{-0.012}$	1.105 ± 0.016
$\log g_\star$ (cgs)	4.478 ± 0.017	4.301 ± 0.013
$L_\star$ ($L_\odot$)	$0.555^{+0.038}_{-0.028}$	1.179 ± 0.037
$T_{\rm eff\star}$ (K)	5326 ± 44	5732 ± 25
[Fe/H]	0.051 ± 0.029	-0.102 ± 0.043
Age (Gyr)	$11.46^{+0.79}_{-1.45}$	11.89 ± 0.60
A_V (mag)	0.258 ± 0.062	0.122 ± 0.024
Distance (pc)	211.1 ± 2.5	347.7 ± 5.1
Binary Star Companion HATS-37B		
$M_\star$ ($M_\odot$)	0.654 ± 0.033	...
$R_\star$ ($R_\odot$)	0.654 ± 0.032	...
$\log g_\star$ (cgs)	4.622 ± 0.023	...
$L_\star$ ($L_\odot$)	0.120 ± 0.023	...
$T_{\rm eff\star}$ (K)	4210 ± 170	...

Note. The listed parameters are those determined through the joint differential evolution Markov Chain analysis described in Section 3. For both systems the RV observations are consistent with a circular orbit, and we assume a fixed circular orbit in generating the parameters listed here. Systematic errors in the bolometric correction tables or stellar evolution models are not included, and likely dominate the error budget.

stellar companion. For the blend modeling we consider five scenarios: (1) a single star with a transiting planet (the *H-p* scenario); (2) an unresolved binary star system with a transiting planet around the brighter stellar component (the *H-p,s* scenario); (3) an unresolved binary star system with a transiting planet around the fainter stellar component (the *H,s-p* scenario); (4) a hierarchical triple star system consisting of a bright star and a fainter eclipsing binary system (the *H,s-s* scenario); and (5) a blend between a bright foreground star, and a background stellar eclipsing binary system (the *H,s-s*$_{BGEB}$ scenario). For each case we perform an initial grid search over the most difficult to optimize parameters to find the global maximum likelihood (ML) fit, and then perform a DEMCMC analysis, initializing the chain near the ML location. As part of this analysis we also predict spectral line bisector span (BS) measurements, and RV measurements from the composite system. These are compared to the observed RV and BS measurements to rule out any blend scenarios that, while consistent with the photometric observations, predict much larger RV and BS variations than observed. For blend scenarios containing a transiting planet, we use these simulated RV observations to determine a scaling factor by which we expect the RV semiamplitude K to be reduced by dilution from the stellar companion. We then use this factor to scale the value of K determined from our *H-p* model of the RV observations to obtain corrected values for the *H-p,s* and *H-s,p* models. We assume a 20% uncertainty on the scaling factor.

For HATS-37 we find that the *H-p,s* scenario provides the best fit to the photometric data, with $\chi^2_{H-p,s} - \chi^2_{H-p} = -296$ and $\chi^2_{H-p,s} - \chi^2_{H,s-s,BGEB} = -166$, and even greater improvements relative to the *H,s-s* and *H,s-p* scenarios. Based on this we conclude that HATS-37 is not a blended stellar eclipsing binary object, but rather is best interpreted as a star with a transiting planet and a fainter, unresolved stellar companion. Note that here the use of the MWDUST Galactic extinction model is critical for coming to this conclusion. When the extinction is allowed to vary without the constraint, we find that the *H,s-s*$_{BGEB}$ scenario provides a slightly better fit to the data than the *H-p,s* model, while the improvement of the *H-p,s* model compared to the *H-p* model is less significant. These models, however, require much greater extinction ($A_V > 3$ mag in the case of the *H,s-s*$_{BGEB}$ model, and $A_V \sim 1$ mag in the case of the *H-p* model) that is at odds with the total line-of-sight extinction of 0.274 mag based on dust maps. The best-fit *H-p,s* model, however, yields $A_V = 0.258 \pm 0.062$ mag, which is in good agreement with the dust maps.

In addition to the photometric evidence for an unresolved stellar companion to HATS-37A, we also find evidence for such a companion in the RV observations. The PFS RVs of this system show a strong linear trend of 0.4539 ± 0.0015 m s^{-1} day^{-1} (Figure 5). We included this trend, together with a Keplerian orbit for the transiting system, in our modeling of the RV observations. If the trend corresponds to the line-of-sight acceleration of HATS-37A due to HATS-37B, then given the estimated mass of $0.654 \pm 0.033\,M_\odot$ from our *H-p,s* model, we can place an upper limit on the current physical separation between the two stars of $a_{AB} < 27.2$ au. This upper limit corresponds to the case where there is no projected separation between the two stars. The maximum projected separation consistent with this acceleration is $a_{AB,\rm proj} < 16.9$ au, corresponding to a maximum current angular separation between the stars of $\theta_{AB} < 0\farcs08$.

For HATS-38 we find that the *H-p*, *H-p,s*, and *H,s-s*$_{BGEB}$ models provide comparable fits to the photometric data, with $\chi^2_{H-p} - \chi^2_{H-p,s} = 7.0$, and $\chi^2_{H-p} - \chi^2_{H,s-s,BGEB} = 5.8$. These differences are comparable to the 1σ scatter in χ^2 for a given model as measured from the Markov Chains, and consistent with the slight improvement in the fit for the *H,s-s*$_{BGEB}$ and *H-p,s* models being solely due to the increased complexity of these models. In this case we make use of the RV and BS observations to rule out the *H,s-s*$_{BGEB}$ model. The simulated HARPS RV and BS observations for the *H,s-s*$_{BGEB}$ model show significantly larger variations than observed, with the simulated RV rms in excess of 200 m s^{-1}, and the simulated BS rms in excess of 300 m s^{-1}. The actual HARPS RV and BS observations have rms scatters of only 12 m s^{-1} and 8 m s^{-1}, respectively, with the RV observations following a Keplerian orbit as expected for the case of a transiting planet system. We can also rule out the *H,s-s* and *H,s-p* models based on the photometry, as these both provide significantly worse fits to the data than the *H-p* model. Since the *H-p,s* model does not provide a significant improvement over the *H-p* model, we choose to adopt the parameters for the system assuming it is a single star with a transiting planet. We place a 95% confidence upper limit on the mass of any unresolved companion star of $M_B < 0.62\ M_\odot$. If we adopted the *H-p,s* model instead, the estimated planetary radius would be smaller by 4%, with a 1σ uncertainty of 5% in the difference. Note that the planet would be smaller due to its host star being smaller, even though the transits would be somewhat diluted.

Figures 1 and 2 compare the best-fit models to the observations for both HATS-37 and HATS-38. The astrometric, spectroscopic, and photometric parameters for both stars are listed in Table 5. Our final set of adopted stellar parameters derived from this analysis is listed in Table 6, while the adopted planetary parameters are listed in Table 7.

Table 7
Adopted Orbital and Planetary Parameters for HATS-37Ab and HATS-38b

Parameter	HATS-37Ab Value	HATS-38b Value
Light curve parameters		
P (days)	4.3315366 ± 0.0000041	4.375021 ± 0.000010
T_c (BJD)[a]	$2458006.80145 \pm 0.00050$	$2457725.16042 \pm 0.00072$
T_{14} (days)[a]	0.1214 ± 0.0010	0.1340 ± 0.0019
$T_{12} = T_{34}$ (days)[a]	0.00822 ± 0.00030	0.00924 ± 0.00035
$a/R_\star$	$12.05^{+0.15}_{-0.23}$	9.81 ± 0.14
$\zeta/R_\star$ [b]	17.65 ± 0.25	16.02 ± 0.25
$R_p/R_\star$	0.0707 ± 0.0018	0.0570 ± 0.0012
b^2	$0.020^{+0.038}_{-0.017}$	$0.227^{+0.027}_{-0.027}$
$b \equiv a\cos i/R_\star$	$0.140^{+0.100}_{-0.092}$	$0.476^{+0.027}_{-0.030}$
i (deg)	89.33 ± 0.45	87.21 ± 0.18
HATSouth dilution factors[c]		
Dilution factor 1	1.000 ± 0.063	0.964 ± 0.036
Dilution factor 2	...	0.90 ± 0.10
Limb-darkening coefficients[d]		
c_1, r	0.5594	0.23 ± 0.13
c_2, r	0.1497	0.35 ± 0.16
c_1, R	0.5328	...
c_2, R	0.1491	...
c_1, i	0.4491	$0.37^{+0.11}_{-0.14}$
c_2, i	0.1683	0.34 ± 0.15
RV parameters		
K (m s^{-1})	13.9 ± 5.8	9.9 ± 1.5
γ (m s^{-1})	6417 ± 0	4144.0 ± 1.5
$\dot{\gamma}$ (m s^{-1} day^{-1})	0.4539 ± 0.0015	...
e[e]	<0.345	<0.122
RV jitter FEROS (m s^{-1})[f]	...	15.3 ± 5.3
RV jitter HARPS (m s^{-1})	<72.8	<2.4
RV jitter PFS (m s^{-1})	8.0 ± 3.0	<5.4
Planetary parameters		
M_p (M_J)	0.099 ± 0.042	0.074 ± 0.011
R_p (R_J)	0.606 ± 0.016	0.614 ± 0.017
$C(M_p, R_p)$ [g]	0.03	-0.06
ρ_p (g cm^{-3})	0.55 ± 0.24	0.403 ± 0.071
$\log g_p$ (cgs)	2.83 ± 0.19	2.691 ± 0.075
a (au)	$0.04913^{+0.00033}_{-0.00023}$	$0.05036^{+0.00030}_{-0.00023}$
$T_{\rm eq}$ (K)	1085^{+16}_{-12}	1294 ± 10
Θ [h]	0.0190 ± 0.0080	0.0136 ± 0.0022
$\log_{10}\langle F\rangle$ (cgs)[i]	$8.495^{+0.026}_{-0.020}$	8.801 ± 0.014

Notes. For all systems we adopt a model in which the orbit is assumed to be circular. See the discussion in Section 3.

[a] Times are in Barycentric Julian date calculated directly from UTC *without* correction for leap seconds. T_c: reference epoch of midtransit that minimizes the correlation with the orbital period. T_{12}: total transit duration, time between first to last contact; $T_{12} = T_{34}$: ingress/egress time, time between first and second, or third and fourth contact.

[b] Reciprocal of the half duration of the transit used as a jump parameter in our MCMC analysis in place of $a/R_\star$. It is related to $a/R_\star$ by the expression $\zeta/R_\star = a/R_\star(2\pi(1 + e\sin\omega))/(P\sqrt{1-b^2}\sqrt{1-e^2})$ (Bakos et al. 2010).

[c] Scaling factor applied to the model transit that is fit to the HATSouth light curves. This factor accounts for dilution of the transit due to blending from neighboring stars and overfiltering of the light curve. These factors are varied in the fit, with independent values adopted for each HATSouth light curve. The factor listed for HATS-37 is for the G567.1 light curve, while for HATS-38 we list the factors for the G561.1, and G561.1.focus light curves in order.

[d] Values for a quadratic law. For HATS-37 the values were determined from the tabulations of Claret (2004) for values of the stellar atmospheric parameters, which varied in the modeling. We list here the values for the spectroscopically determined atmospheric parameters. For HATS-38, the limb-darkening parameters were directly varied in the fit, using the tabulations from Claret et al. (2012, 2013) and Claret (2018) to place prior constraints on their values. The difference in treatment between the two systems stems from differences in the software used to model the blended system HATS-37 and the unblended system HATS-38.

[e] The 95% confidence upper limit on the eccentricity determined when $\sqrt{e}\cos\omega$ and $\sqrt{e}\sin\omega$ are allowed to vary in the fit.

[f] Term added in quadrature to the formal RV uncertainties for each instrument. This is treated as a free parameter in the fitting routine. In cases where the jitter is consistent with zero, we list its 95% confidence upper limit.

[g] Correlation coefficient between the planetary mass M_p and radius R_p estimated from the posterior parameter distribution.

[h] The Safronov number is given by $\Theta = \frac{1}{2}(V_{\rm esc}/V_{\rm orb})^2 = (a/R_p)(M_p/M_\star)$ (see Hansen & Barman 2007).

[i] Incoming flux per unit surface area, averaged over the orbit.

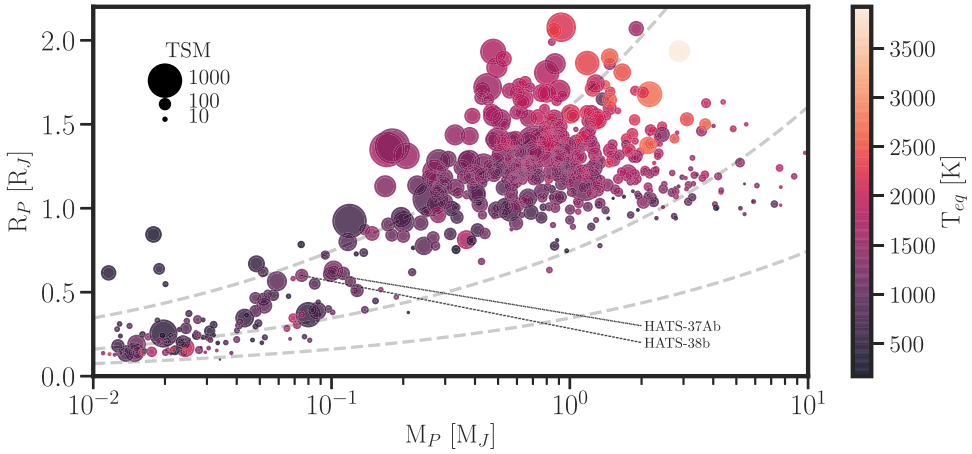

Figure 6. Mass–radius diagram for the population of well-characterized transiting planets (Southworth 2011). The points corresponding to HATS-37Ab and HATS-38b are indicated with dashed lines. The color represents the equilibrium temperature of the planet, while the size scales down with the transmission spectroscopy metric as defined by Kempton et al. (2018). The dashed gray lines correspond to isodensity curves for 0.3, 3 and 30 g cm^{-3}, respectively.

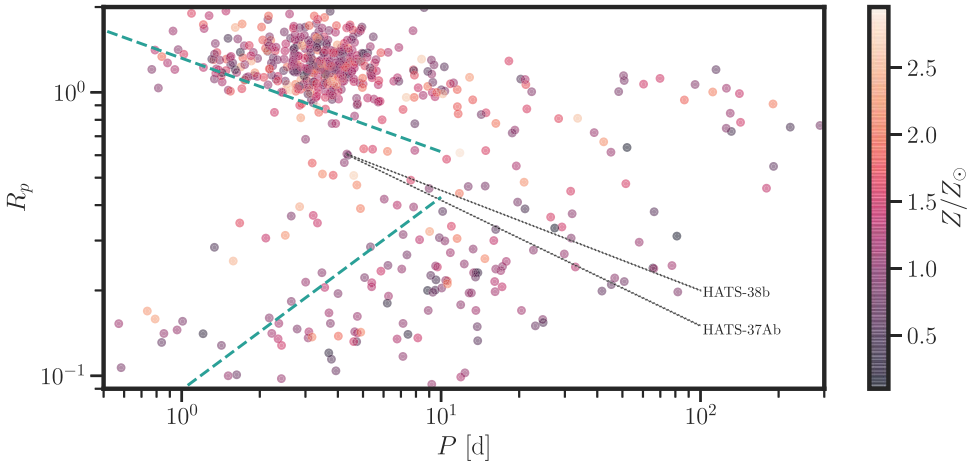

Figure 7. Period–radius diagram for the population of well-characterized transiting planets. The points corresponding to HATS-37Ab and HATS-38b are indicated with dotted black lines. The dashed cyan lines mark the boundaries of the Neptune desert as defined by Mazeh et al. (2016). The points are color-coded according to the metallicity of the host star.

4. Discussion

We put HATS-37Ab and HATS-38b in the context of the population of known, well-characterized[21] transiting exoplanets in Figure 6, where we show a scatter plot of planetary mass versus planetary radius, coding with color the equilibrium temperature. Both planets have a relatively low density close to 0.3 g cm^{-3}, which among with their other properties translates into a transmission spectroscopy metric (TSM, Kempton et al. 2018) of ≈120 for HATS-37Ab and ≈165 for HATS-38b. The latter figure makes HATS-38b an attractive target among the currently known set of transiting Neptunes for transmission spectroscopy. Both targets populate a region in the mass–radius plane that is sparsely populated and where the transition between gas giants and the population of smaller planets occurs. We note that both HATS-37Ab and HATS-38b are among the lowest-mass planets found from ground-based wide-field surveys to date, joining a select group of systems uncovered by such surveys with masses $M_p \lesssim 0.1 M_J$: HAT-P-26 b ($0.059 \pm 0.007\,M_J$, Hartman et al. 2011), NGTS-4 b ($0.0648 \pm 0.0094\,M_J$, West et al. 2019), HAT-P-11 b ($0.0736 \pm 0.0047\,M_J$, Bakos et al. 2010; Yee et al. 2018), and WASP-166 b ($0.101 \pm 0.005\,M_J$, Hellier et al. 2019).

In Figure 7 we show the population of well-characterized planets in the period–radius plane, where HATS-37Ab and HATS-38b are extremely similar. In this figure we show the region defined as the Neptune desert by Mazeh et al. (2016). While they do not lie in the region with $P \lesssim 3$ days and $0.4 \lesssim (R_p/R_J) \lesssim 0.8$ that is essentially devoid of planets, both HATS-37Ab and HATS-38b lie within the region defined as the Neptune desert, which has an intrinsically low occurrence rate of planets.

When we consider parameters other than planetary mass and radius and consider the properties of the host stars, the properties of HATS-37Ab and HATS-38b emerge as being particularly rare. Dong et al. (2018) used a large sample of stellar parameters obtained with the Large Sky Area Multi-Object Fiber Spectroscopic Telescope (LAMOST) to further characterize the Neptune desert region. Their study revealed a dearth of planets in the radius range $6 \lesssim (R_p/R_\oplus) \lesssim 10$, which they termed the Saturn valley, and a population of hot

[21] We use the catalog of well-characterized planets of Southworth (2011). The catalog is kept updated online at https://www.astro.keele.ac.uk/jkt/tepcat/ and the data we used were retrieved in 2019 November. We restrict the sample to systems whose fractional error on their planetary masses are <50%, and planetary radii are <25%.

Neptunes with radii $2 \lesssim (R_p/R_\oplus) \lesssim 6$, which are rare (occurrence rate of ≈1% for FGK stars) and whose occurrence is correlated with metallicity in the sense that hot Neptunes appear preferentially around metal-rich stars. In fact, Dong et al. (2018) found the great majority of the hot Neptunes in their sample to be hosted by stars with [Fe/H] $\geqslant 0.1$. Both HATS-37Ab and HATS-38b have radii $\approx 6.7 R_\oplus$, making them large specimens for hot Neptunes and veering into the Saturn valley as defined by Dong et al. (2018). More strikingly, HATS-38 has an estimated metallicity of ≈−0.1, making it a very metal-poor star to host a hot Neptune given the expected occurrence rate at that metallicity of order $\sim 10^{-3}$ (Dong et al. 2018; see their Figure 4). Even if the metallicity was as high as ≈0.05, as allowed at the $\approx 3.5\sigma$ level, the expected occurrence rate is $\lesssim 5 \times 10^{-3}$. Thus, we can see that HATS-37Ab and HATS-38b contribute a new pair of exoplanetary systems with uncommon properties and showcase the continuing contributions of wide-field ground-based surveys to better map the variety of landscapes present in the exoplanetary realm.

Development of the HATSouth project was funded by NSF MRI grant NSF/AST-0723074, operations have been supported by NASA grants NNX09AB29G, NNX12AH91H, and NNX17AB61G, and follow-up observations have received partial support from grant NSF/AST-1108686. A.J., R.B., and V.S. acknowledge support from project IC120009 "Millennium Institute of Astrophysics (MAS)" of the Millenium Science Initiative, Chilean Ministry of Economy. A.J. acknowledges additional support from FONDECYT project 1171208. R.B. acknowledges additional support from FONDECYT Postdoctoral Fellowship Project No. 3180246. L.M. acknowledges support from the Italian Minister of Instruction, University and Research (MIUR) through FFABR 2017 fund. T.H. acknowledges support from the European Research Council under the Horizon 2020 Framework Program via the ERC Advanced Grant Origins 83 24 28. K.P. acknowledges support from NASA grant 80NSSC18K1009.2 This work is based on observations made with ESO Telescopes at the La Silla Observatory. This paper also makes use of observations from the LCOGT network. Some of this time was awarded by NOAO. We acknowledge the use of the AAVSO Photometric All-Sky Survey (APASS), funded by the Robert Martin Ayers Sciences Fund, and the SIMBAD database, operated at CDS, Strasbourg, France. Operations at the MPG 2.2 m Telescope are jointly performed by the Max Planck Gesellschaft and the European Southern Observatory. We thank the MPG 2.2 m telescope support team for their technical assistance during observations. This work has made use of data from the European Space Agency (ESA) mission Gaia (https://www.cosmos.esa.int/gaia), processed by the Gaia Data Processing and Analysis Consortium (DPAC, https://www.cosmos.esa.int/web/gaia/dpac/consortium). Funding for the DPAC has been provided by national institutions, in particular the institutions participating in the Gaia Multilateral Agreement. This research has made use of the NASA Exoplanet Archive, which is operated by the California Institute of Technology, under contract with the National Aeronautics and Space Administration under the Exoplanet Exploration Program.

Facilities: HATSouth, LCOGT, FTS, CTIO:0.9 m, Danish 1.54 m Telescope (DFOSC), Swope, Max Planck:2.2 m (FEROS), ESO:3.6 m (HARPS), Euler1.2 m (Coralie), ATT (WiFeS), AAT (CYCLOPS), Magellan:Clay (PFS), VLT: Kueyen (UVES), NTT (Astralux Sur), Gaia.

ORCID iDs

A. Jordán https://orcid.org/0000-0002-5389-3944
G. Á. Bakos https://orcid.org/0000-0001-7204-6727
D. Bayliss https://orcid.org/0000-0001-6023-1335
J. Bento https://orcid.org/0000-0002-9832-9271
W. Bhatti https://orcid.org/0000-0002-0628-0088
R. Brahm https://orcid.org/0000-0002-9158-7315
N. Espinoza https://orcid.org/0000-0001-9513-1449
J. D. Hartman https://orcid.org/0000-0001-8732-6166
L. Mancini https://orcid.org/0000-0002-9428-8732
K. Penev https://orcid.org/0000-0003-4464-1371
M. Rabus https://orcid.org/0000-0003-2935-7196
P. Sarkis https://orcid.org/0000-0001-8128-3126
V. Suc https://orcid.org/0000-0001-7070-3842
M. de Val-Borro https://orcid.org/0000-0002-0455-9384
G. Zhou https://orcid.org/0000-0002-4891-3517
R. P. Butler https://orcid.org/0000-0003-1305-3761
J. Crane https://orcid.org/0000-0002-5226-787X
T. G. Tan https://orcid.org/0000-0001-5603-6895
J. J. Wallace https://orcid.org/0000-0001-6135-3086

References

Barentsen, G., Hedges, C., Vinícius, Z., et al. 2019, KeplerGO/lightkurve: Lightkurve v1.0b29 (Version v1.0b29), Zenodo, doi:10.5281/zenodo.2565212
Bakos, G. Á, Bayliss, D., Bento, J., et al. 2020, AJ, 159, 267
Bayliss, D., Zhou, G., Penev, K., et al. 2013, AJ, 146, 113
Beaugé, C., & Nesvorný, D. 2013, ApJ, 763, 12
Borucki, W. J., Koch, D., Basri, G., et al. 2010, Sci, 327, 977
Bovy, J., Rix, H.-W., Green, G. M., Schlafly, E. F., & Finkbeiner, D. P. 2016, ApJ, 818, 130
Brahm, R., Jordán, A., & Espinoza, N. 2017a, PASP, 129, 034002
Brahm, R., Jordán, A., Hartman, J., & Bakos, G. 2017b, MNRAS, 467, 971
Brown, T. M., Baliber, N., Bianco, F. B., et al. 2013, PASP, 125, 1031
Butler, R. P., Marcy, G. W., Williams, E., et al. 1996, PASP, 108, 500
Claret, A. 2004, A&A, 428, 1001
Claret, A. 2018, A&A, 618, A20
Claret, A., Hauschildt, P. H., & Witte, S. 2012, A&A, 546, A14
Claret, A., Hauschildt, P. H., & Witte, S. 2013, A&A, 552, A16
Crane, J. D., Shectman, S. A., & Butler, R. P. 2006, Proc. SPIE, 6269, 626931
Crane, J. D., Shectman, S. A., Butler, R. P., et al. 2010, Proc. SPIE, 7735, 773553
Crane, J. D., Shectman, S. A., Butler, R. P., Thompson, I. B., & Burley, G. S. 2008, Proc. SPIE, 7014, 701479
Bakos, G. Á, Csubry, Z., Penev, K., et al. 2013, PASP, 125, 154
Dong, S., Xie, J.-W., Zhou, J.-L., Zheng, Z., & Luo, A. 2018, PNAS, 115, 266
Dopita, M., Hart, J., McGregor, P., et al. 2007, Ap&SS, 310, 255
Espinoza, N., Bayliss, D., Hartman, J. D., et al. 2016, AJ, 152, 108
Hansen, B. M. S., & Barman, T. 2007, ApJ, 671, 861
Hartman, J. D., Bakos, G. Á, Bayliss, D., et al. 2019, AJ, 157, 55
Hartman, J. D., Bayliss, D., Brahm, R., et al. 2015, AJ, 149, 166
Hartman, J. D., Bakos, G. Á, Kipping, D. M., et al. 2011, ApJ, 728, 138
Hellier, C., Anderson, D. R., Triaud, A. H. M. J., et al. 2019, MNRAS, 488, 3067
Jenkins, J. M., Twicken, J. D., McCauliff, S., et al. 2016, Proc. SPIE, 9913, 99133E
Jordán, A., Brahm, R., Bakos, G. Á, et al. 2014, AJ, 148, 29
Kaufer, A., & Pasquini, L. 1998, Proc. SPIE, 3355, 844
Kempton, E. M.-R., Bean, J. L., Louie, D. R., et al. 2018, PASP, 130, 114401
Kovács, G., Bakos, G., & Noyes, R. W. 2005, MNRAS, 356, 557
Kovács, G., Zucker, S., & Mazeh, T. 2002, A&A, 391, 369
Marigo, P., Girardi, L., Bressan, A., et al. 2017, ApJ, 835, 77
Mayor, M., Pepe, F., Queloz, D., et al. 2003, Msngr, 114, 20
Mazeh, T., Holczer, T., & Faigler, S. 2016, A&A, 589, A75
Mohler-Fischer, M., Mancini, L., Hartman, J. D., et al. 2013, A&A, 558, A55
Owen, J. E., & Lai, D. 2018, MNRAS, 479, 5012

Pál, A. 2012, MNRAS, 421, 1825
Penev, K., Bakos, G. Á, Bayliss, D., et al. 2013, AJ, 145, 5
Queloz, D., Mayor, M., Udry, S., et al. 2001, Msngr, 105, 1
Rabus, M., Jordán, A., Hartman, J. D., et al. 2016, AJ, 152, 88
Ricker, G. R., Winn, J. N., Vanderspek, R., et al. 2015, JATIS, 1, 014003
Southworth, J. 2011, MNRAS, 417, 2166
Stassun, K. G., Oelkers, R. J., Paegert, M., et al. 2019, AJ, 158, 138
Szabó, G. M., & Kiss, L. L. 2011, ApJL, 727, L44
Bakos, G. Á, Torres, G., Pál, A., et al. 2010, ApJ, 710, 1724
West, R. G., Gillen, E., Bayliss, D., et al. 2019, MNRAS, 486, 5094
Wheatley, P. J., West, R. G., Goad, M. R., et al. 2018, MNRAS, 475, 4476
Yee, S. W., Petigura, E. A., Fulton, B. J., et al. 2018, AJ, 155, 255
Zacharias, N., Finch, C. T., Girard, T. M., et al. 2013, AJ, 145, 44
Zechmeister, M., & Kürster, M. 2009, A&A, 496, 577
Ziegler, C., Law, N. M., Baranec, C., et al. 2018, AJ, 156, 259